Closing the Gaps: Multifunctional Molecular Filling for Highly Efficient and Stable Inverted Perovskite Solar Cells

*Ruihao Su[1]†, Boxin Jiao[1]†, Junjie Zhou[1]†, Minghao Li[1], Yiran Ye[1], Yongbin Jin[1], Shuyang Wang[1], Junliang Yang[2], Chenyi Yi[1]**

1. State Key Laboratory of Power System, Department of Electrical Engineering, Tsinghua University, Beijing 100084, China

2. Hunan Key Laboratory for Super-microstructure and Ultrafast Process, School of Physics, Central South University, Changsha 410083, China

† These authors contributed equally.

* Corresponding Authors Email: yicy@mail.tsinghua.edu.cn

Materials and methods

Materials

All the chemicals were purchased from commercial sources and used without further purification unless otherwise stated. Dimethylformamide (DMF), dimethyl sulfoxide (DMSO) and chlorobenzene (CB) were purchased from Acros. Ethanol (EtOH) and isopropyl alcohol (IPA) were obtained from Aladdin (China). Chloromethyltrichlorosilane (CMS) and methyltrichlorosilane (MS) were purchased from Adamas. 1-chlorooctane was purchased from Bide Pharmatech Ltd. Formamidinium iodide (FAI) and lead iodide (PbI_2) were purchased from Xi'an Huada Zhiyuan Technology Co., Ltd. Propane-1,3-diammonium iodide ($PDAI_2$) was purchased from TCI. C_{60} was purchased from Xi'an Yuri Solar Co., Ltd. The hole transporting materials (4-(7H-dibenzo[c,g]carbazol-7-yl)butyl)phosphonic acid (4PADCB), methylammonium chloride (MACl) and methylammonium iodide (MAI) were synthesized in our lab.

Methods

DFT calculations

All the calculations were performed in the framework of the density functional theory (DFT) with the projector augmented plane-wave method, as implemented in the Vienna Ab-initio Simulation Package (VASP).[1,2] The generalized gradient approximation (GGA) proposed by Perdew, Burke, and Ernzerhof was selected for the exchange-correlation potential.[3] The long-range van der Waals interaction was described by the DFT-D3 approach.[4] The plane wave cut-off energy of 400 eV was adopted, the energy convergence accuracy was set to 1×10^{-5} eV/atom, and the force acting on each atom was not greater than 0.1 eV/Å. The Brillouin zone was integrated with k-point grids of 2 × 2 × 1. All quantum chemical calculations were performed using Gaussian 09.[5] The initial structures were optimized using the b3lyp density functional with the 6-311G(d, p) basis set. Optimized geometries were verified by frequency calculations at the same level of theory as that used for geometry optimization. The interaction energy was calculated by the following equation: $E_{int} = E_{combination} - E_{split\ structure1} - E_{split\ structure2}$. For the calculation of energy barriers in ion migration transition states, VASP and VTST packages were used, and the climbing-image nudged elastic band (CI-NEB) method was employed to map the minimum energy path using five images (including the initial and final states).[6,7] The energy of the initial structure was set as the reference energy (0 eV). Energy barriers were computed from the energy difference between the minimum state and saddle point.[8]

All ab initio molecular dynamic (AIMD) simulations were carried out using CP2K code.[9] The electronic structure was described using Perdew–Burke-Ernzerhof (PBE) functional with D3 correction within the Gaussian and plane waves (GPW) framework.[4,10] Molecular orbitals of the valence electrons were expanded into DZVP-MOLOPT-SR-GTH basis sets.[11] The temperature was set to 300 K. The plane-wave basis set was truncated at the energy cutoff of 400 Ry and REL_CUTOFF = 30 Ry for this model. The temperature was controlled by a CSVR thermostat with a time constant of 50 fs, and the volume was kept constant by applying an NVT ensemble.[12] The time step of the dynamics was set to 1 fs. The visualization and calculation of radial distribution functions (RDF) were performed using Visual Molecular Dynamics (VMD).[13]

Device fabrication

The FTO substrates were patterned by laser etching and then ultrasonically cleaned with detergent, deionized water, ethanol and isopropanol sequentially and then treated with UV-ozone for 20 min before hole transporting layer deposition. The as-prepared substrates were transferred to an N_2-filled glove box ($O_2 < 0.1$ ppm, $H_2O < 0.1$ ppm). The self-assembled monolayer (SAM) was formed by spin-coating a 4PADCB solution (0.5 mg/mL in ethanol) onto the FTO substrate at 5000 rpm for 30 s, followed by thermal annealing at 100 °C for 10 min. For CMS modification, the CMS solution was spin-coated on the SAM at 5000 rpm and annealed at 100 °C for 5 min. Then, a solvent wash was performed by spin-coating (DMF volume: DMSO volume = 9:1) and annealed at 100 °C for 5 min. CMS (20 μL/mL, 2 vol%) was dissolved in 1-chlorooctane. For perovskite layers, 1.5 M PbI_2 solution with 6 mg/mL RbCl in DMF and DMSO (volume ratio 9:1) was first spin-coated onto the CMS layer at 1500 rpm. After annealing at 70 °C for 1 min, organic ammonium salt (FAI: MACl = 90 mg: 13 mg in 1 ml IPA) solution was then spun onto the PbI_2 layer at 2000 rpm and then annealed at 50 °C for 1 min in N_2-filled glove box. Then the films were annealed at 150 °C for 15 min in an ambient environment (relative humidity < 30%). For the posttreatment process, the cooled perovskite films were treated with 0.5 mg/mL $PDAI_2$/IPA solution at 5000 rpm for 30 s and then annealed at 100 °C for 10 min. For the electronic transporting layer, C_{60} was deposited by thermally evaporating 270 Å at a rate of 0.3 Å/s. Then ALD SnO_2 was deposited by 150 cycles. Finally, a 100 nm Ag back contact was deposited by thermal evaporation at a rate of 0.8 Å/s.

The fabrication process for the one-step devices is identical to that of the two-step devices, except for the perovskite layer. For the one-step method, a 1.6 M perovskite ($Cs_{0.05}MA_{0.05}FA_{0.9}PbI_3$) solution with 10 mol% excess PbI_2 and 13 mol% MACl dissolved in DMF: DMSO (volume ratio 3:1) was shaken and spin-coated on glass/FTO/4PADCB substrate at 4700 rpm for 42 s. Chlorobenzene (200 μL) was dripped 5 s before the end of the spinning, followed by annealing at 120 °C for 20 min.

Characterization

X-ray photoelectron spectroscopy (XPS) measurements were performed on a Kratos Axis Ultra DLD X-ray photoelectron spectrometer by using a monochromatized Al Kα source (hν = 1486.6 eV).

Conductive atomic force microscopy (C-AFM) measurements were performed using an Asylum Research Cypher S (Oxford Instruments) with a Pt-coated conductive tip under air atmosphere. The C-AFM was conducted in conductive AFM mode.

Nuclear magnetic resonance (NMR) measurements: ^{1}H NMR spectra were acquired using a Bruker AVANCE III 600 MHz NMR spectrometer. The sample powder was dissolved in deuterated dimethyl sulfoxide (DMSO-d_6) and filtered. The solution was then transferred into a clean NMR tube for testing.

Fourier transform infrared (FTIR) spectra were obtained by Bruker Vertex 70 infrared spectrometer in the ATR-FTIR mode.

Scanning electron microscope (SEM) images of the perovskite film were obtained using a Zeiss Merlin.

X-ray diffraction (XRD) measurements of perovskite films were conducted on a Rigaku SmartLab (copper Kα, λ = 1.54 Å, 150 mA, 40 kV).

Photoluminescence (PL) and time-resolved photoluminescence (TRPL) spectra results were collected on an Edinburgh FLSP920 system. The TRPL intensity decay spectra (Fig. S10) were fitted with a bi-exponential

decay function as equation 1, where I_0 is the decay constant, A_1 and A_2 are decay amplitudes, τ_1 is the fast decay time reflecting the interface charge extraction and τ_2 is the slow decay time reflecting the trap-assisted nonradiative charge recombination. The mean fluorescence lifetime τ_{avg} was calculated from the equation 2. The mean fluorescence lifetime (τ_{avg}) was 481.45 ns for the control group and 681.25 ns for the target group.

$$I(t) = I_0 + A_1 exp(-t/\tau_1) + A_2 exp(-t/\tau_2) \quad (1)$$

$$\tau_{avg} = (A_1\tau_1^2 + A_2\tau_2^2)/(A_1\tau_1 + A_2\tau_2) \quad (2)$$

Sun *J-V* curves measurements of the perovskite solar cells were performed under simulated AM 1.5G illumination (Newport AAA solar simulator) with a Keithley 2400 source meter. An aperture area of 0.1 cm^2 was achieved by using a dark metal mask. The measurement was conducted in air using unencapsulated devices. All the devices were measured under a sweep mode of reverse scan (from 1.2 to 0 V) and forward scan (from 0 to 1.2 V) with the scan rate of 0.03 V/s. Dark *J-V* curves were based on the *J-V* characteristics with the light source off.

The incident photon-to-electron conversion efficiency (IPCE), electroluminescence (EL), transient photocurrent (TPC), and transient photovoltage (TPV) tests were measured using an ARKEO platform (Cicci research Italy). A non-reflective metal mask with an aperture area of 0.1 cm^2 was used to cover the active area of the device to avoid light scattering through the sides.

Photoluminescence quantum yield (PLQY) measurements. The excitation light for PL measurement was coupled into the integrating sphere through an optical fiber. The quasi-Fermi level splitting (QFLS) of multilayer device stacks was calculated based on PLQY.[14] $QFLS_{rad}$ represents the radiative limit of QFLS. Comparing the QFLS of stacks with and without CMS layer can quantify the non-radiative losses at the interface between the perovskite layer and the transport layer. To understand the origin of non-radiative recombination losses in the device, we calculated the QFLS of samples using the following relationship between QFLS and PLQY:[15]

$$QFLS = k_B T \times \ln(PLQY \times \frac{J_G}{J_{0,rad}}) \quad (3)$$

$$QFLS_{rad} = QFLS - k_B T \times \ln(PLQY) \quad (4)$$

Where k_B and T represent Boltzmann constant and temperature, respectively. J_G is the current density under 1 sun illumination, and $J_{0,rad}$ is the dark radiative recombination saturation current density. According to the detailed balance theory:

$$J_{0,rad} = q\int_0^\infty EQE_{PV}(E)\Phi_{BB}(E)dE \quad (5)$$

$$\Phi_{BB}(E) = \frac{2\pi E^2}{h^3c^2} \times \frac{1}{exp\left(\frac{E}{k_B T}\right)-1} \quad (6)$$

Where q, EQE_{PV}, Φ_{BB}, E, h and c represent elementary charge, photovoltaic external quantum efficiency, black-body radiative spectrum, photon energy, Planck constant, and speed of light in vacuum, respectively. The value of $J_{0,rad}$ is 1.50×10^{-20} mA/cm^2 and 1.77×10^{-20} mA/cm^2 for devices with and without CMS, respectively.

Light-intensity-dependent open-circuit voltage.

$$V_{oc} = \frac{nkT}{q} In\phi + b \quad (7)$$

where k is the Boltzmann constant, T is the temperature, q is the elementary charge, and n reflects the ideal factor.

Fill factor (FF) loss analysis. The FF losses in high-performing PSCs are determined by two main factors, non-radiative loss and charge transport loss. $FF_{SQ\text{-}limit}$ will be calculated according to the Shockley–Queisser limit. The maximum FF (FF_{max}) can be calculated according to the following equation:

$$\mathrm{FF_{max}} = \frac{v_{OC} - \ln(v_{OC} + 0.72)}{\mathrm{v_{OC}} + 1} \tag{8}$$

$$v_{OC} = \frac{qV_{OC}}{nkT} \tag{9}$$

where n is ideality factor, k is Boltzmann constant, T is temperature, q is elementary charge. The ideality factors were extracted from the V_{OC} as a function of light intensity.

The trap density tests measured by space-charge-limited current method (SCLC) were calculated using equation 10:

$$N_{defect} = \frac{2V_{TFL}\varepsilon_0\varepsilon_r}{qL^2} \tag{10}$$

Where the voltage of the trap-filled limit (V_{TFL}) is defined as the voltage value at the intersection point of the two fitting lines representing the Ohmic contact and trap-filled regime. ε_r and ε_0 are the relative permittivity of the perovskite and the vacuum, respectively. L is the thickness of the films, and q is the electron charge. The SCLC tests were measured on devices with the configuration of glass/FTO/SAM/perovskite/Spiro-OMeTAD/Au (hole-only devices), with a voltage range from 0 to 1.2 V in the dark.[16] In the preparation of hole-only devices, Spiro-OMeTAD hole transport layer solution was composed of 72.3 mg of Spiro-OMeTAD and 1 mL of chlorobenzene with additives, including 17.5 μL of Li-TFSI salt solution in acetonitrile (520 mg/mL) and 28.5 μL of 4-tert-butylpyridine. The solution was deposited onto the perovskite film by spin-coating at 4000 rpm for 20 seconds. After being stored in a dry box for 24 hours, the devices were thermally evaporated with a 100 nm Au layer. The remaining steps were identical to those in the preparation method for perovskite solar cells (PSCs).

All stability tests were conducted without encapsulation. The aging stability of unencapsulated perovskite films and perovskite solar cells was carefully monitored in a N_2 atmosphere. For the maximum power point tracking (MPPT) under continuous illumination following the ISOS[17] protocol, we used white LEDs under N_2 conditions.

Time-of-flight secondary ion mass spectrometry (TOF-SIMS) was performed using an ION TOF-SIMS 5-100 system.

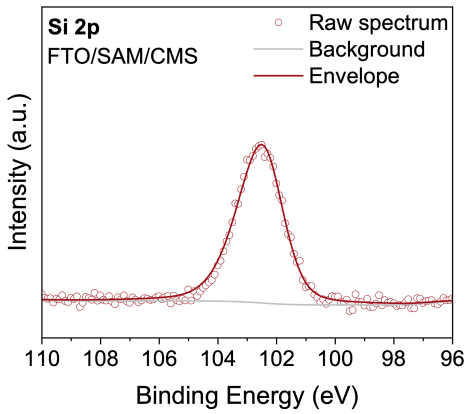

Figure S1. Si 2p XPS spectra of FTO/SAM/CMS surfaces.

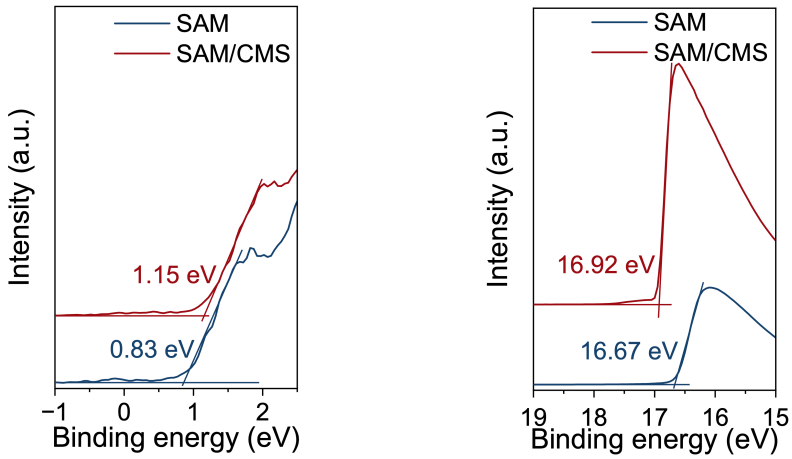

Figure S2. UPS spectra: valence-band region (left); secondary-electron cut-off region (right) for SAM film and SAM/CMS film.

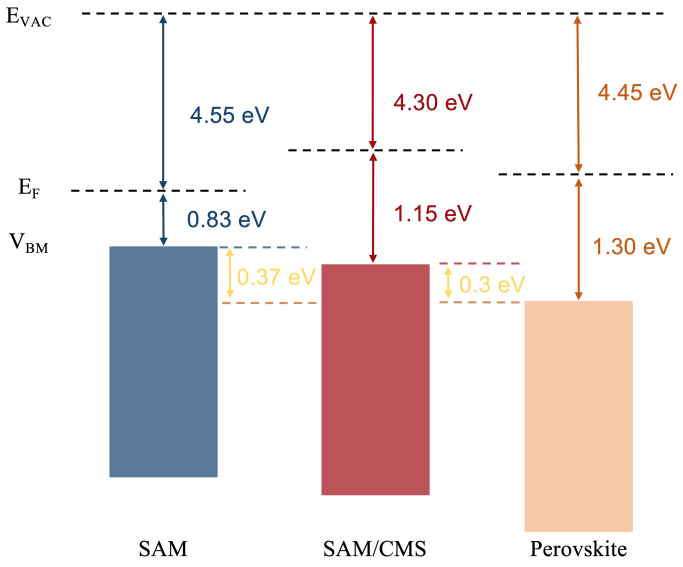

Figure S3. Energy levels of SAM film, SAM/CMS film and perovskite film.

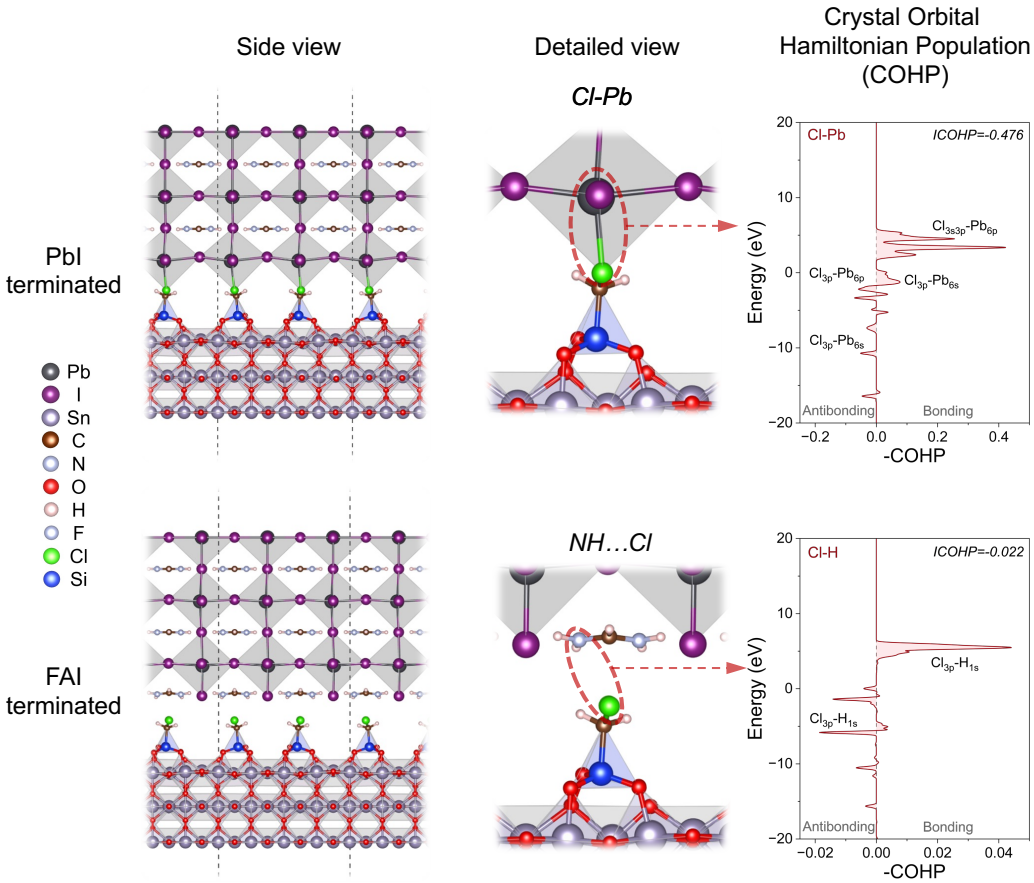

Figure S4. DFT-optimized heterojunction structures (FTO/CMS molecule/PVK) with two distinct perovskite terminations (PbI- and FAI-terminated), detailed views of the corresponding binding sites, and the crystal orbital Hamiltonian population (COHP) analysis of the Cl–Pb/Cl–H interactions.

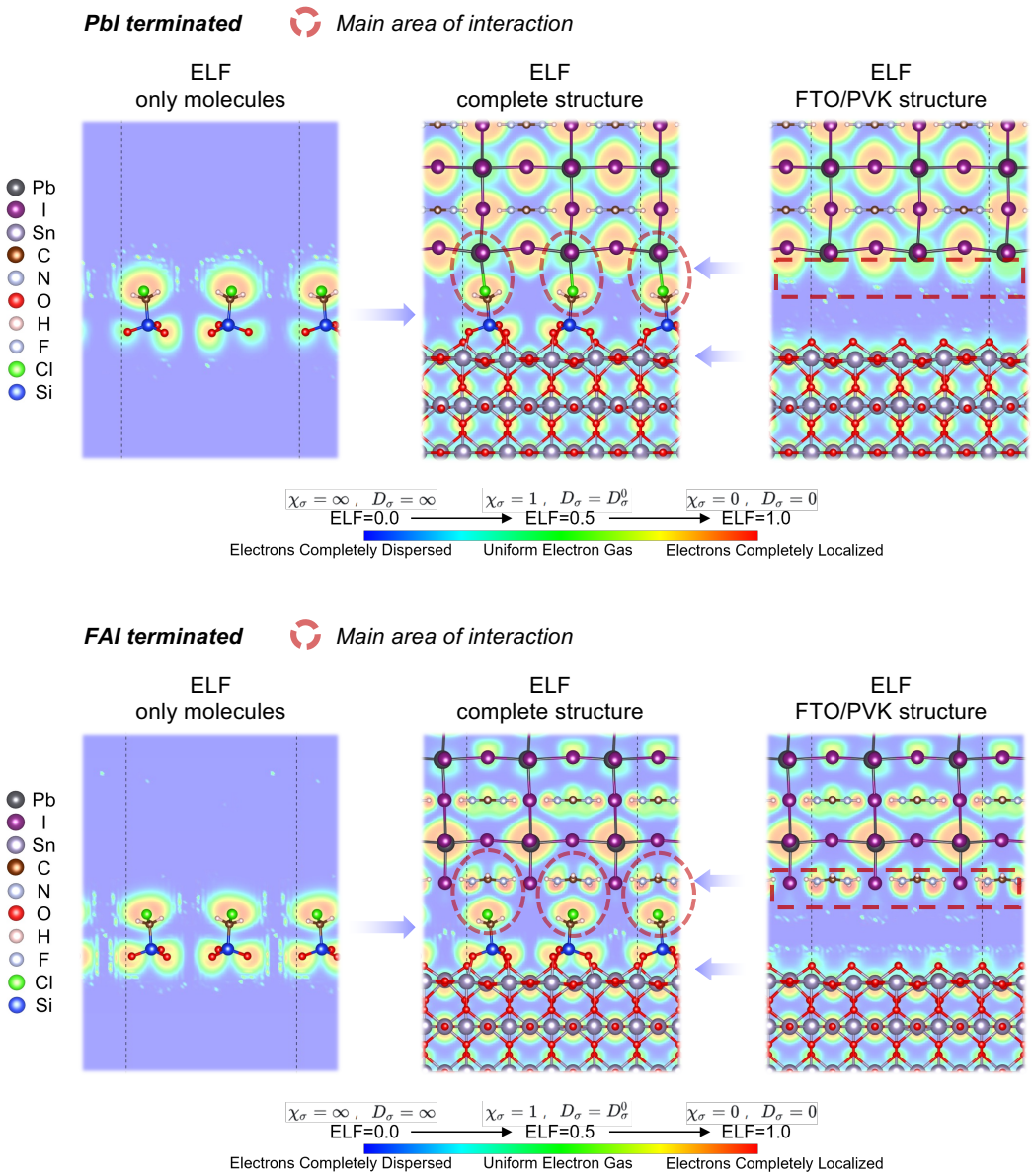

Figure S5. Electron localization function (ELF) of the DFT-optimized heterojunction structures. Three distinct ELF calculations were performed for each configuration: only molecules, FTO/PVK structure, and the complete structure. The red circles highlight the specific interaction sites between the CMS molecules and the PVK layer.

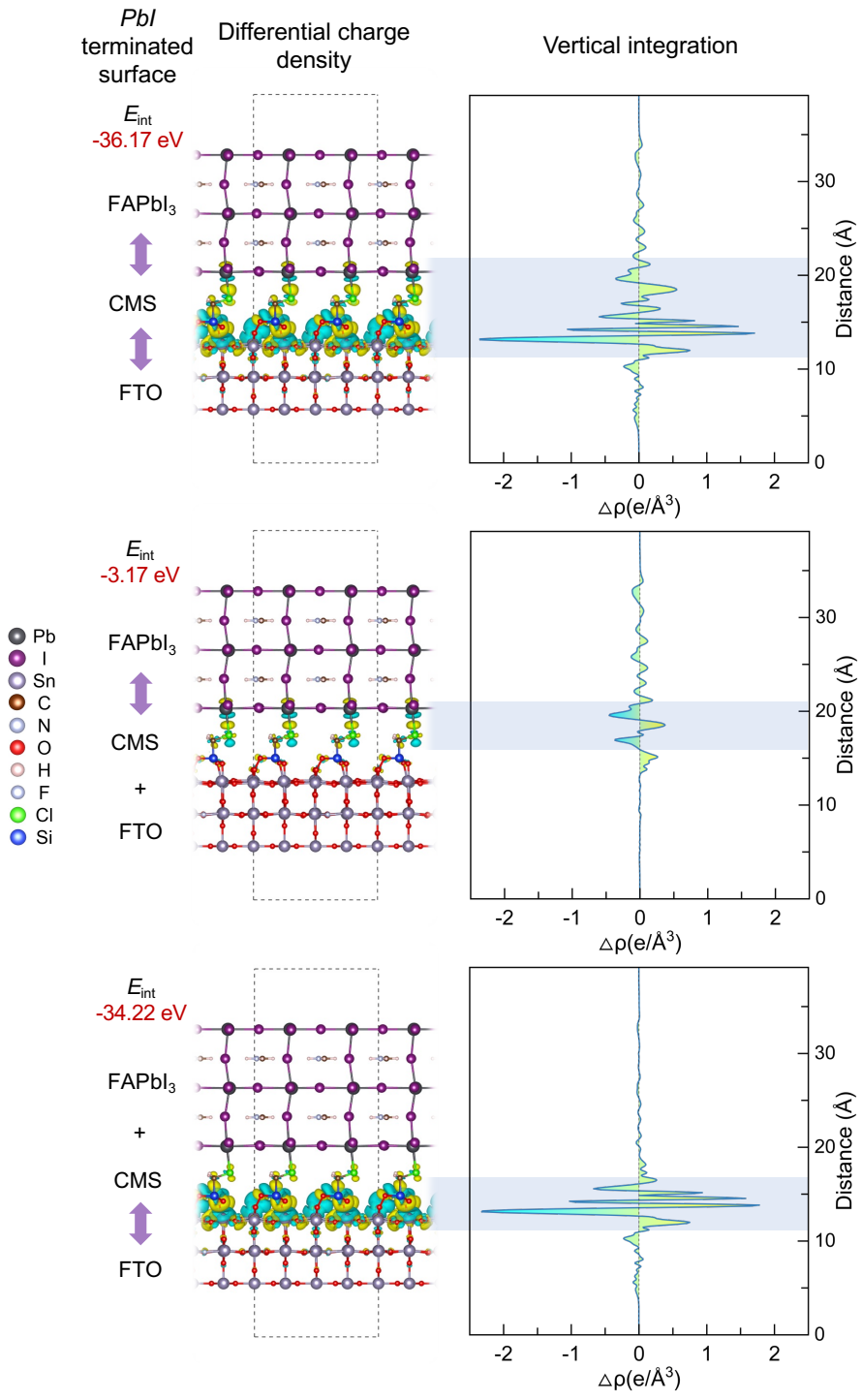

Figure S6. Differential charge density and its planar-averaged profile for the DFT-optimized, PbI-terminated heterojunction structure. Three differential charge density calculations were performed: between CMS and $FAPbI_3$+FTO, between $FAPbI_3$ and CMS+FTO, and between $FAPbI_3$+CMS and FTO.

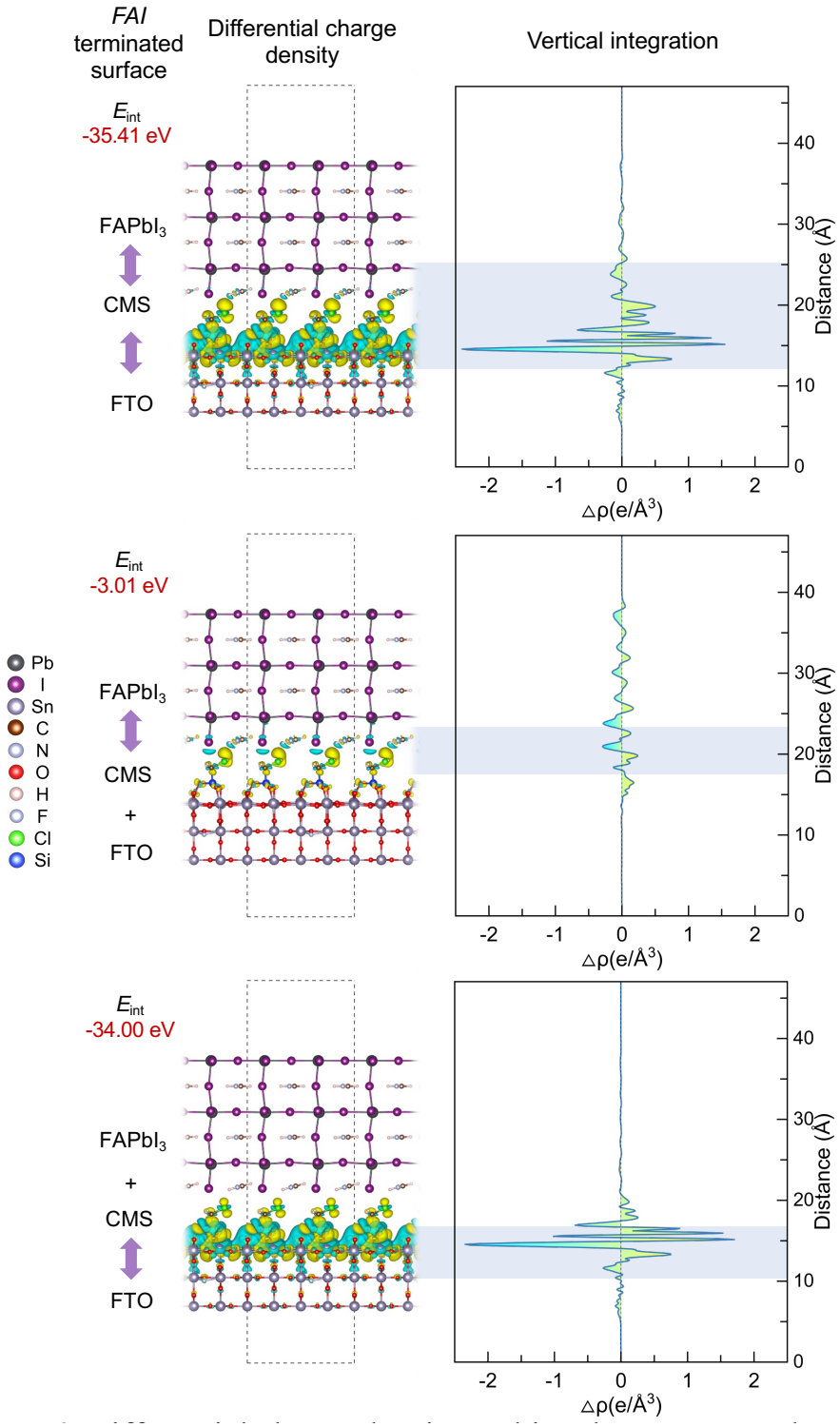

Figure S7. Differential charge density and its planar-averaged profile for the DFT-optimized, FAI-terminated heterojunction structure. Three differential charge density calculations were performed: between CMS and $FAPbI_3$+FTO, between $FAPbI_3$ and CMS+FTO, and between $FAPbI_3$+CMS and FTO.

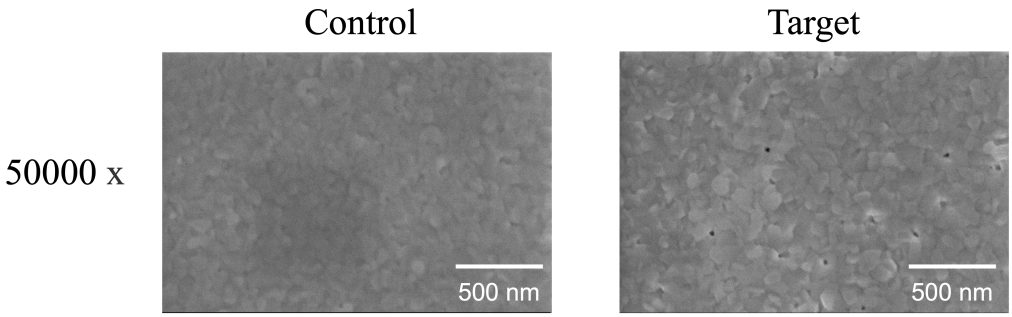

Figure S8. Top-view SEM images of control PbI_2 film and target PbI_2 film.

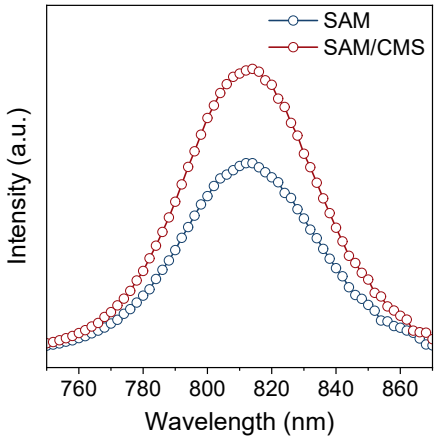

Figure S9. Steady-state photoluminescence spectra of control and CMS-modified PVK films.

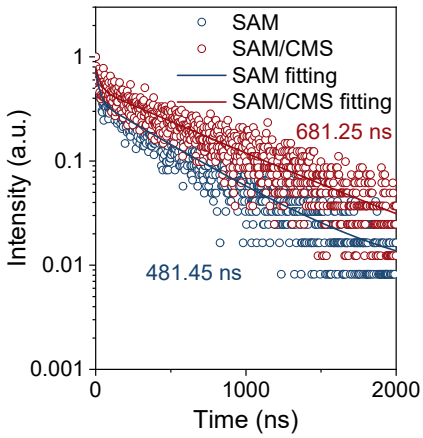

Figure S10. Time-resolved photoluminescence decay spectra of control and CMS-modified PVK films.

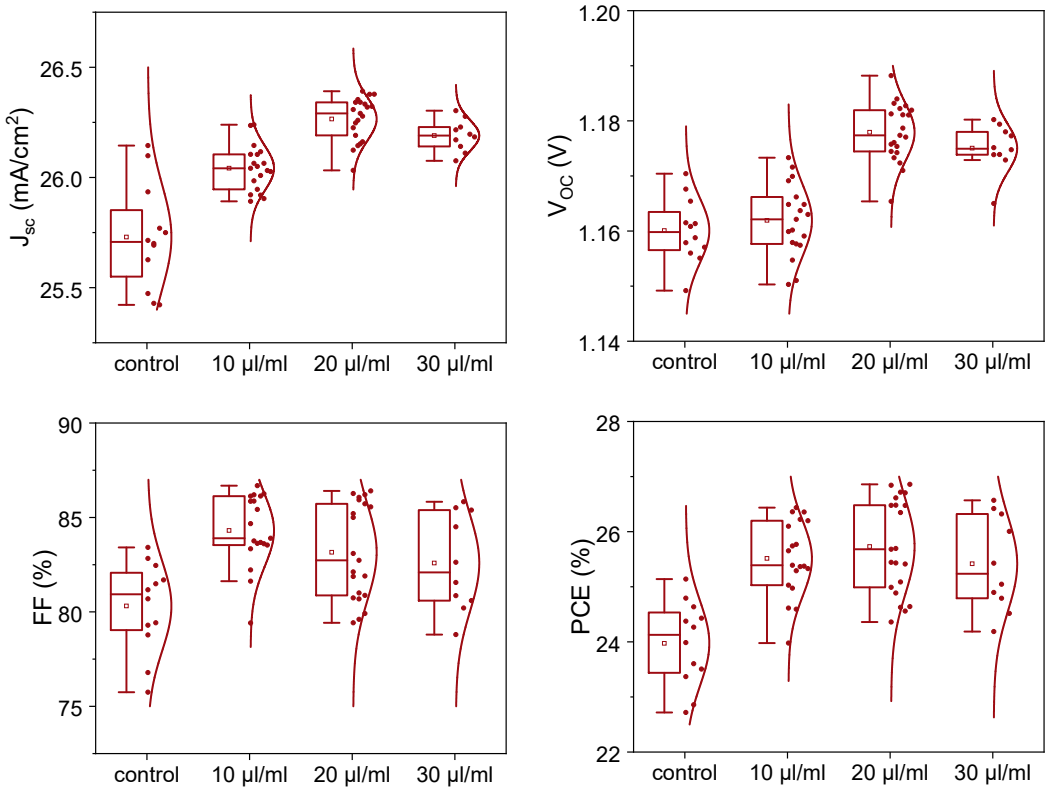

Figure S11. Photovoltaic parameters of J_{SC}, V_{OC}, FF and PCE for CMS-based PSCs plotted against CMS concentration.

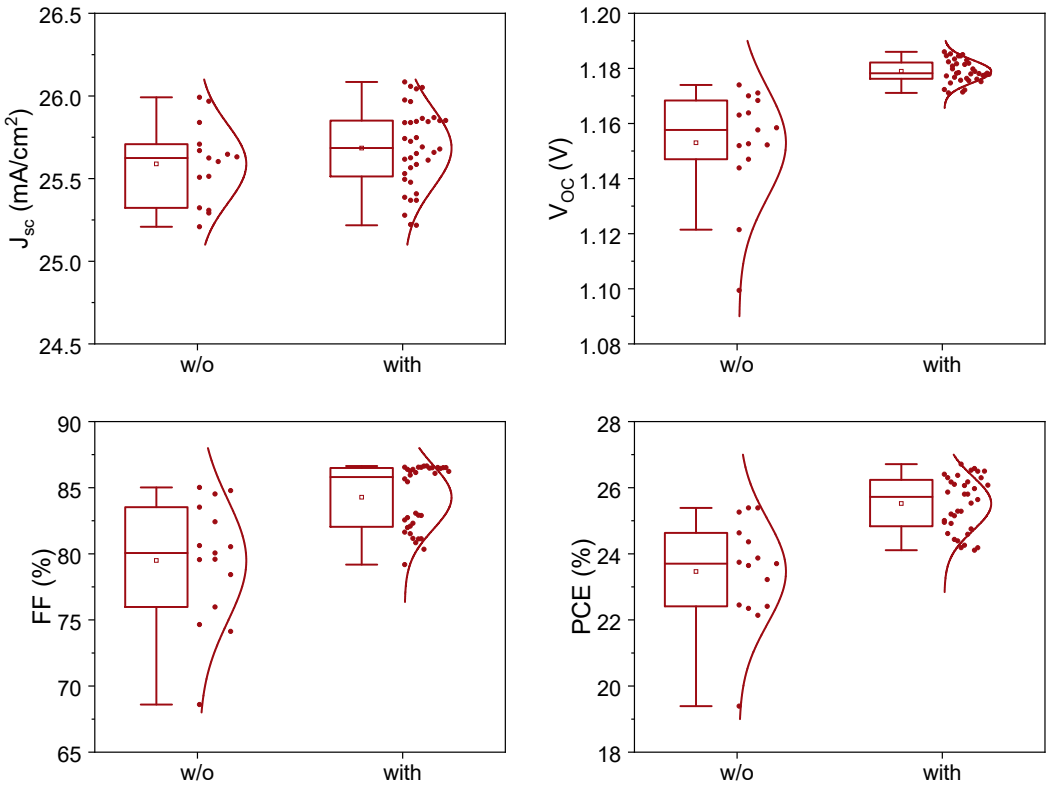

Figure S12. Comparison of photovoltaic parameters between PSCs fabricated by one-step method without and with CMS modification.

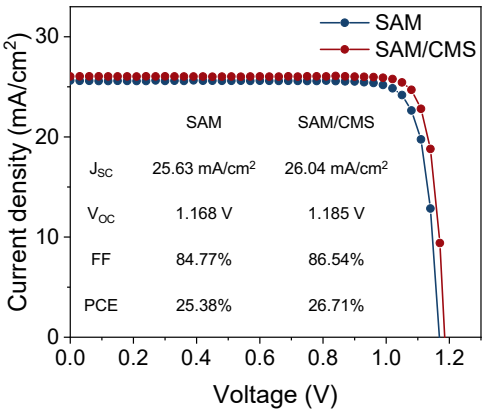

Figure S13. *J–V* curves (reverse scan) of the champion PSCs without and with CMS via one-step method.

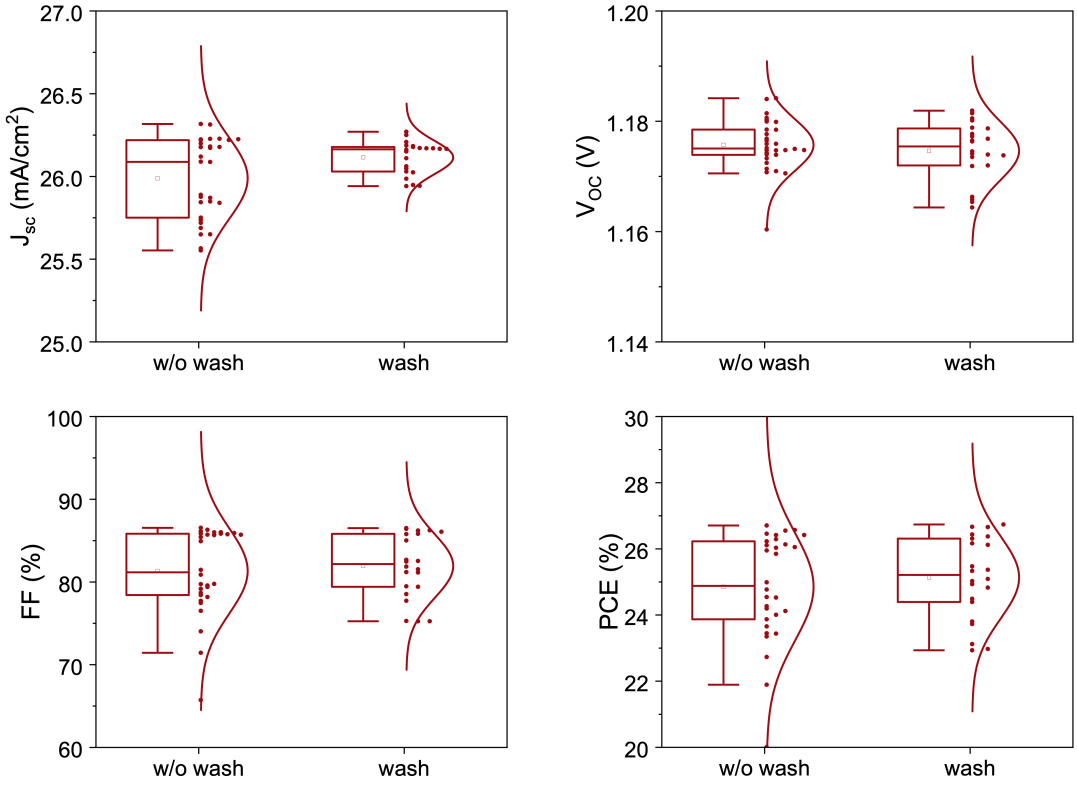

Figure S14. The photovoltaic parameters of the devices without and with washing after CMS modification.

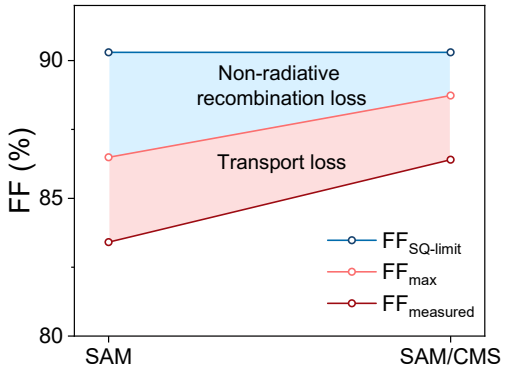

Figure S15. FF loss analysis of PSCs without and with CMS.

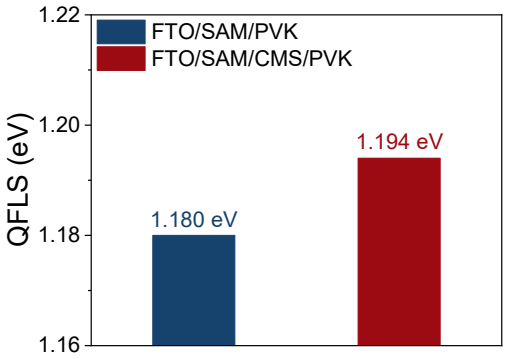

Figure S16. Quasi-Fermi level splitting (QFLS) diagram of the FTO/SAM/PVK films without and with CMS.

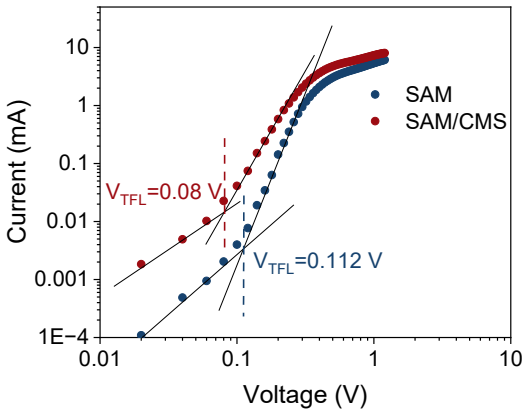

Figure S17. Space-charge-limited current (SCLC) versus voltage curves for the hole-only devices without and with CMS. (Structure: glass/FTO/SAM/PVK/Spiro-OMeTAD/Au).

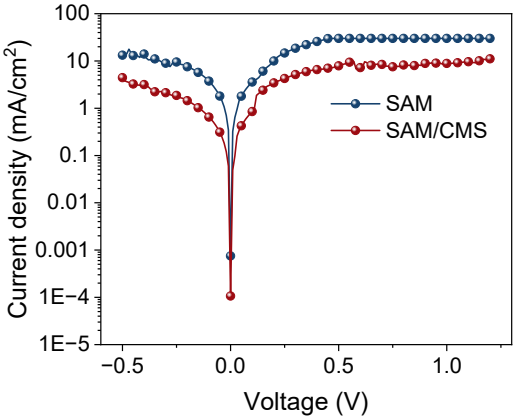

Figure S18. Dark *J*–*V* curves of the devices without and with CMS.

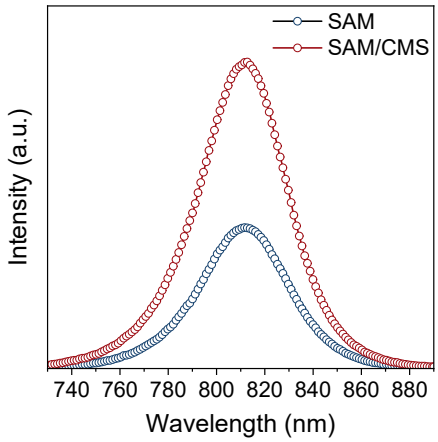

Figure S19. Electroluminescence spectra of PSCs without and with CMS.

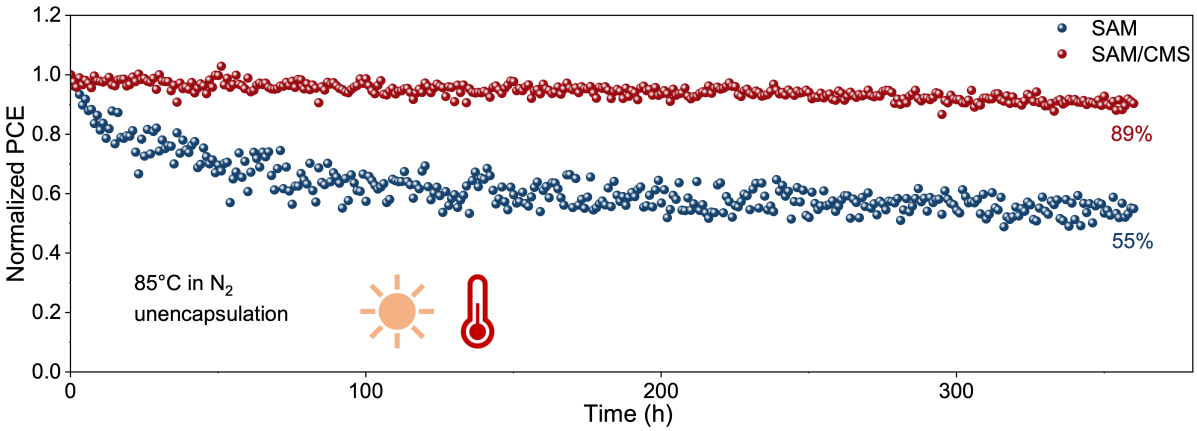

Figure S20. Maximum power point tracking (MPPT) of the PSCs under continuous 1-sun light soaking at 85°C.

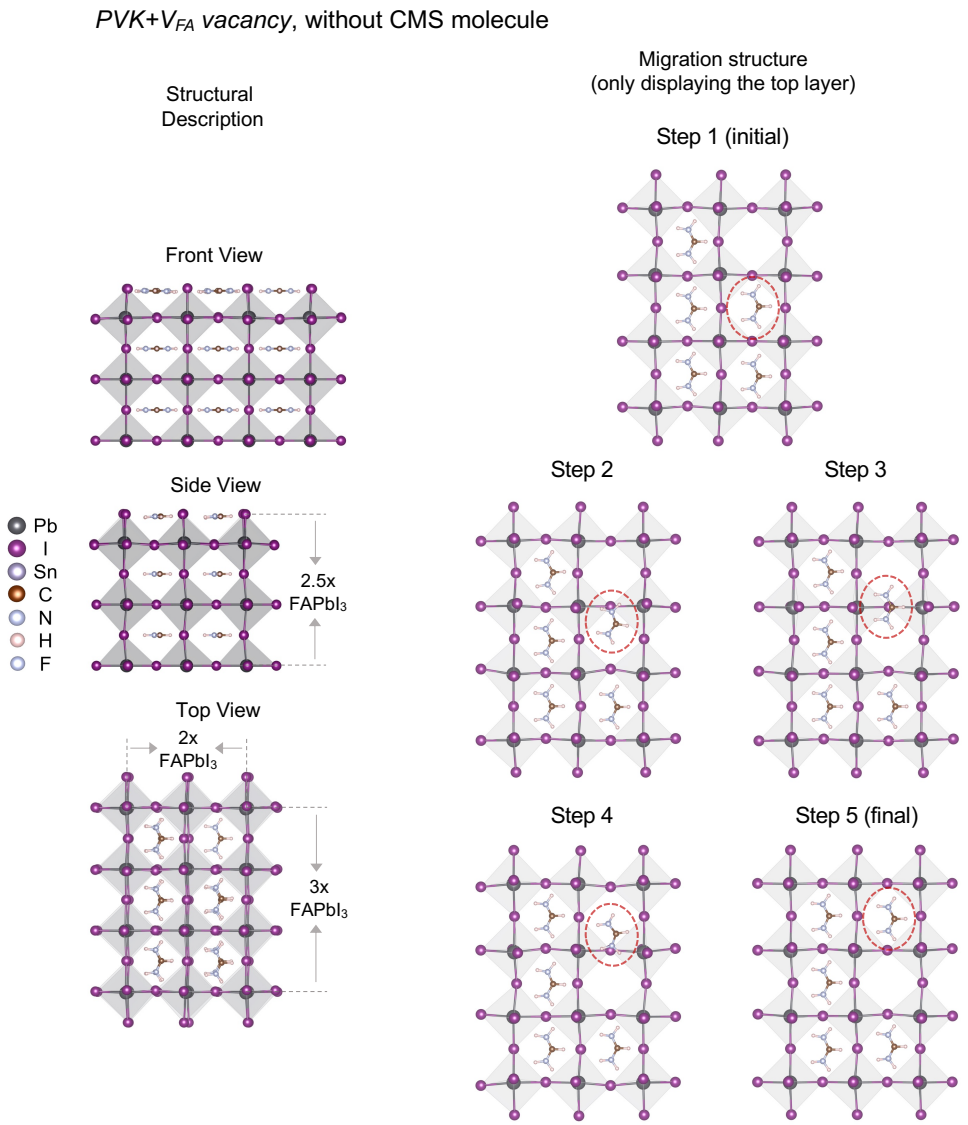

Figure S21. Schematic of the crystal structure and key-frame snapshots (optimized) for the FA^+ ion migration transition state, calculated using DFT with the climbing-image nudged elastic band (CI-NEB) method. The perovskite crystal features an FAI-terminated surface, with an intentional V_{FA} (FA vacancy) introduced to provide the migration site.

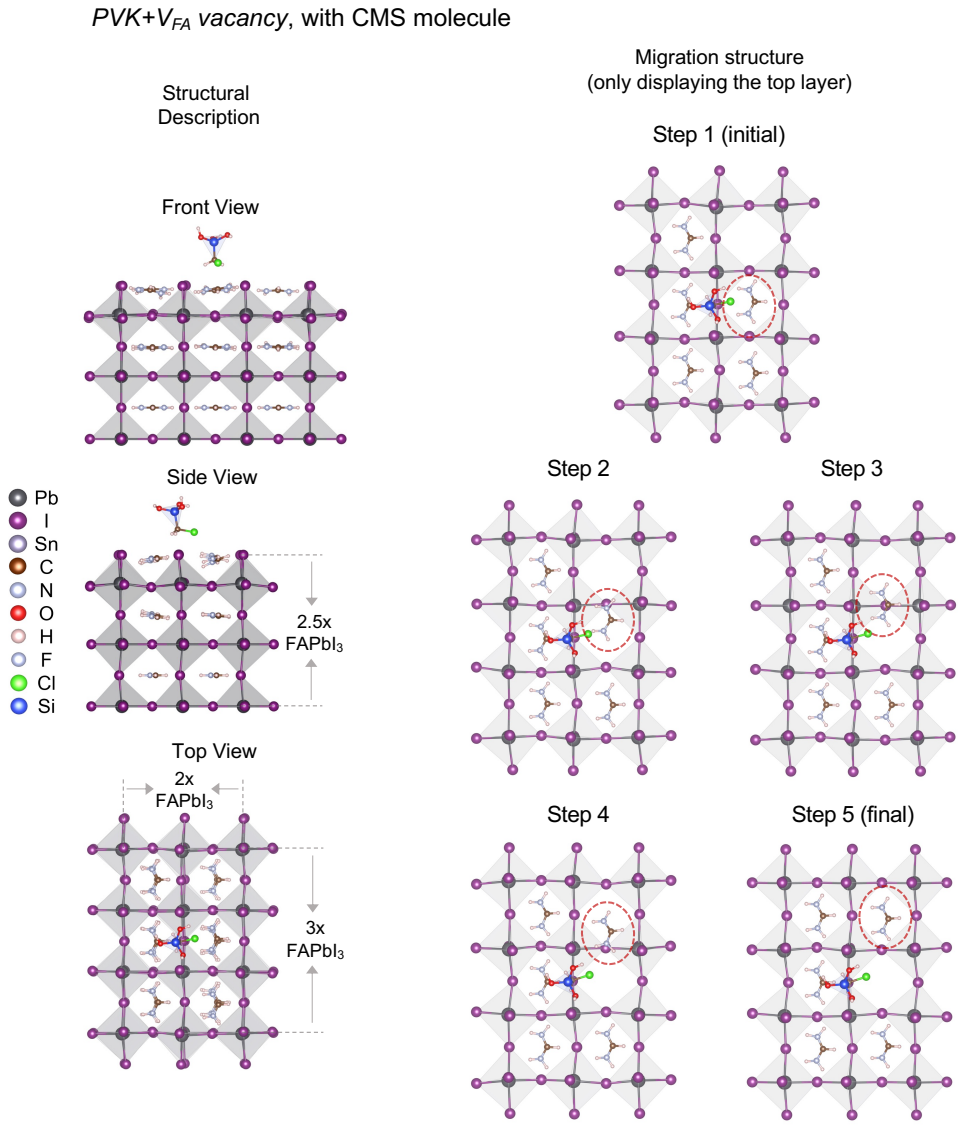

Figure S22. Schematic of the crystal structure and key-frame snapshots (optimized) for the FA^+ ion migration transition state in the presence of the CMS molecule, calculated using DFT with the climbing-image nudged elastic band (CI-NEB) method. The perovskite crystal features an FAI-terminated surface, with an intentional V_{FA} (FA vacancy) introduced to provide the migration site.

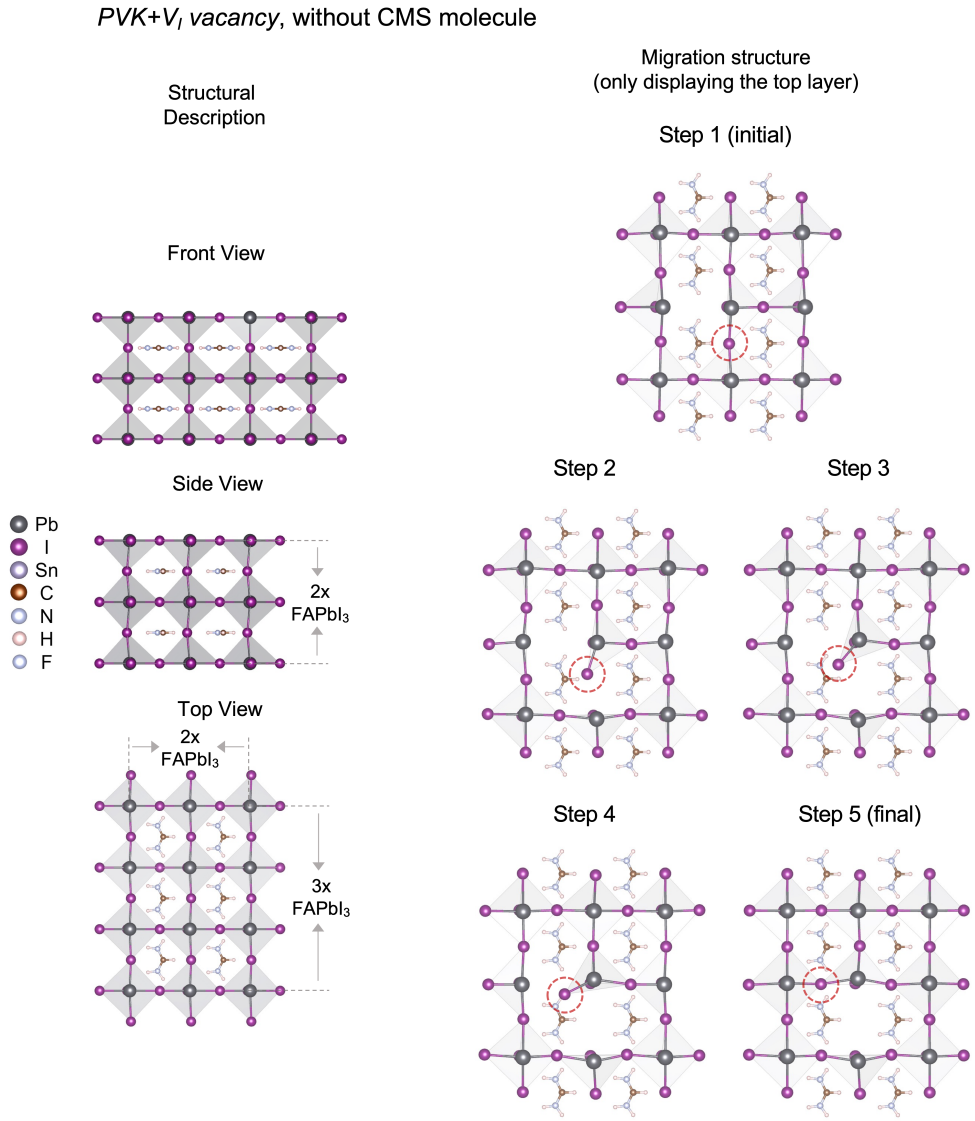

Figure S23. Schematic of the crystal structure and key-frame snapshots (optimized) for the I^- ion migration transition state, calculated using DFT with the climbing-image nudged elastic band (CI-NEB) method. The perovskite crystal features an FAI-terminated surface, with an intentional V_I (I vacancy) introduced to provide the migration site.

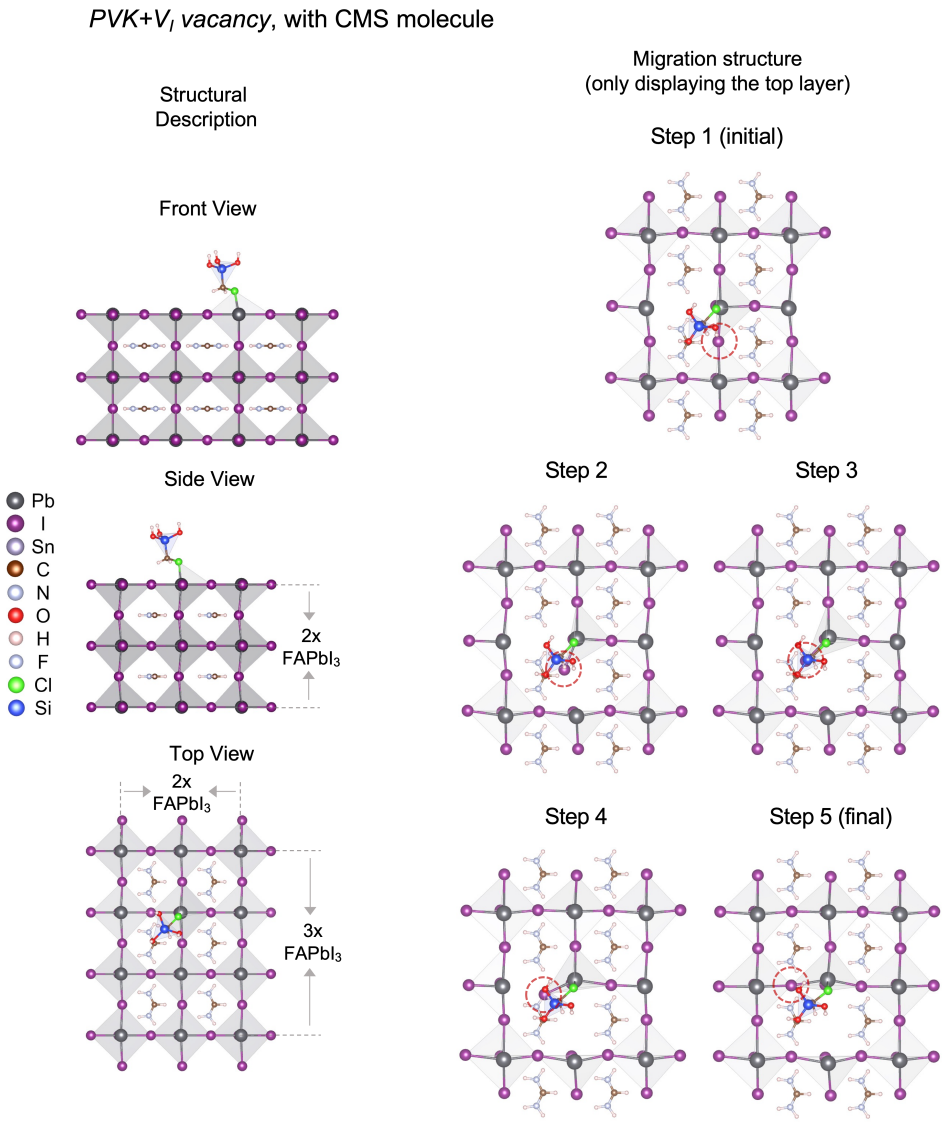

Figure S24. Schematic of the crystal structure and key-frame snapshots (optimized) for the I^- ion migration transition state in the presence of the CMS molecule, calculated using DFT with the climbing-image nudged elastic band (CI-NEB) method. The perovskite crystal features an FAI-terminated surface, with an intentional V_I (I vacancy) introduced to provide the migration site.

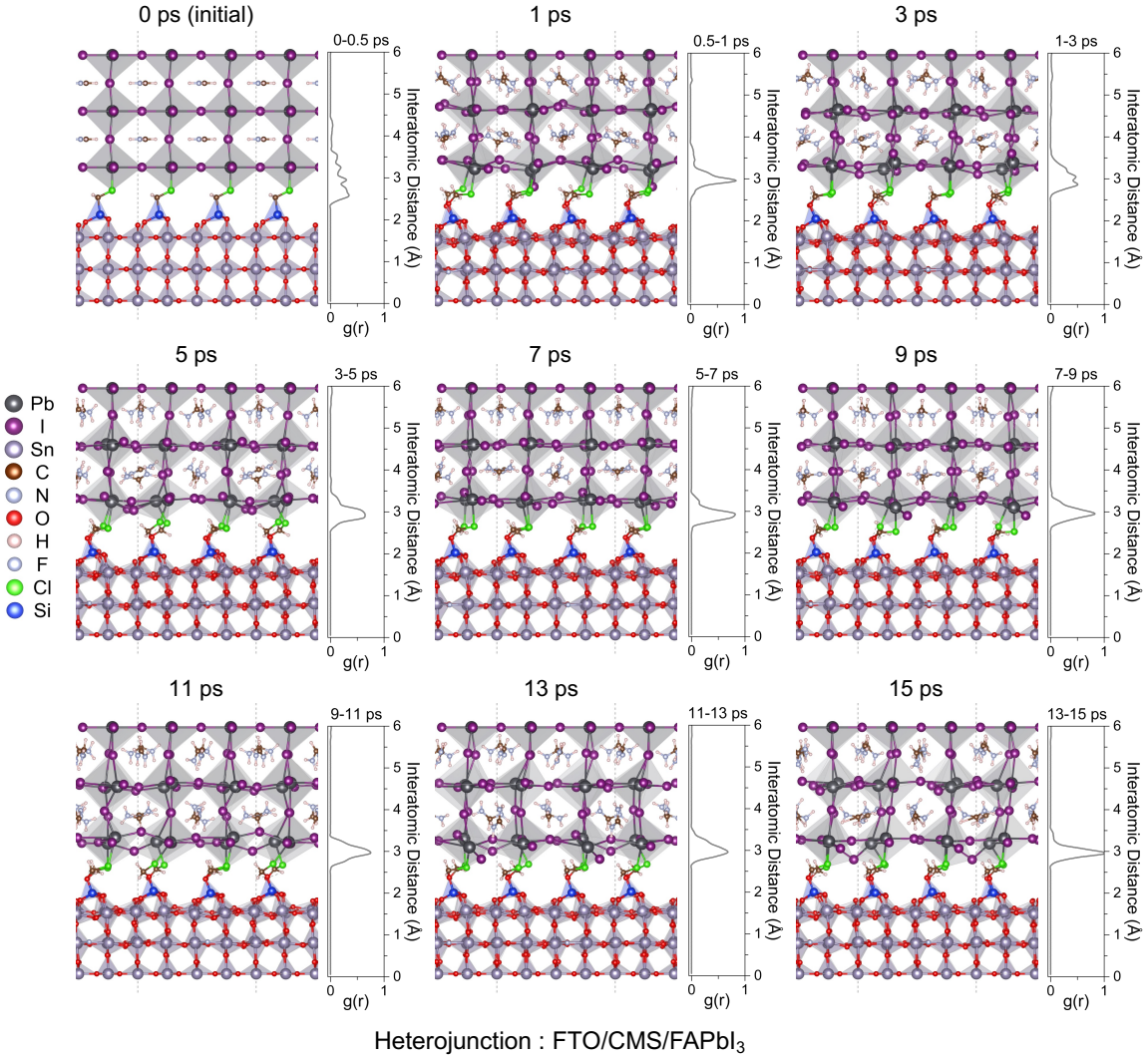

Figure S25. Snapshots of the heterojunction structure and the corresponding radial distribution function (RDF) from a 15 ps ab initio molecular dynamics (AIMD) simulation in the NVT ensemble.

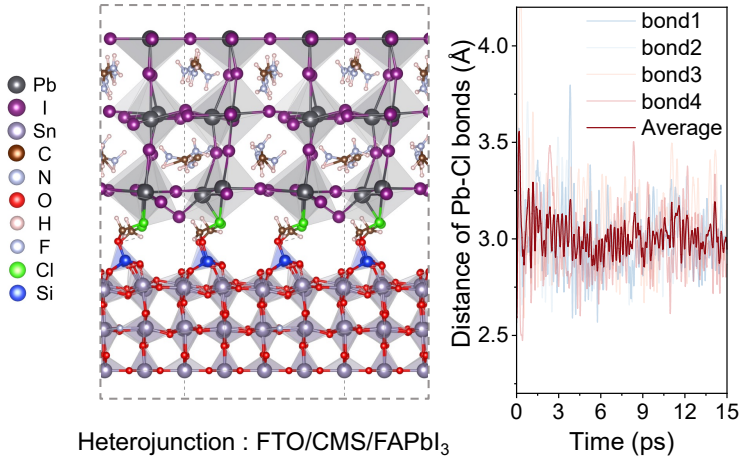

Figure S26. Snapshot of the heterojunction structure after a 15 ps ab initio molecular dynamics (AIMD) simulation in the NVT ensemble. Evolution of the four Cl–Pb bond lengths and their average length over the AIMD simulation time.

Table S1. Fitting parameters for the O 1s XPS peak of FTO/SAM film.

Peak name	Binding Energy (eV)	Area (CPS.eV)	Atomic (%)
Sn-O-Sn	530.9	225618	52
Sn-O-P	532.2	145627	34
Sn-OH	533.1	60777	14

Table S2. Fitting parameters for the O 1s XPS peak of FTO/SAM/CMS film.

Peak name	Binding Energy (eV)	Area (CPS.eV)	Atomic (%)
Sn-O-Sn	530.9	165257	45
Sn-O-Si	532.0	54974	15
Sn-O-P	532.2	132723	37
Sn-OH	533.1	13414	3

Table S3. The photovoltaic parameters for optimal devices in the target group and the control group, respectively.

	J_{SC}	V_{OC}	FF	PCE	Hysteresis
SAM Forward scan	25.69 mA/cm^2	1.161 V	78.78%	23.49%	
SAM Reverse scan	25.75 mA/cm^2	1.170 V	83.41%	25.14%	0.069
SAM/CMS Forward scan	26.22 mA/cm^2	1.183 V	81.89%	25.41%	
SAM/CMS Reverse scan	26.16 mA/cm^2	1.188 V	86.40%	26.85%	0.056

Reference

1. G. Kresse and J. Furthmuller, *Phys. Rev. B*, 1996, **54**, 11169-11186.

2. G. Kresse and D. Joubert, *Phys. Rev. B*, 1999, **59**, 1758–1775.

3. J. P. Perdew, K. Burke and Y. Wang, *Phys. Rev. B*, 1996, **54**, 16533–16539.

4. S. Grimme, *J. Comput. Chem.*, 2006, **27**, 1787–1799.

5. G. W. T. M. J. Frisch, H. B. Schlegel, G. E. Scuseria, M. A. Robb, J. R. Cheeseman, G. Scalmani, V. Barone, B. Mennucci, G. A. Petersson, H. Nakatsuji, M. Caricato, X. Li, H. P. Hratchian, A. F. Izmaylov, J. Bloino, G. Zheng, J. L. Sonnenberg, M. Hada, M. Ehara, K. Toyota, R. Fukuda, J. Hasegawa, M. Ishida, T. Nakajima, Y. Honda, O. Kitao, H. Nakai, T. Vreven, J. A. Montgomery, Jr., J. E. Peralta, F. Ogliaro, M. Bearpark, J. J. Heyd, E. Brothers, K. N. Kudin, V. N. Staroverov, R. Kobayashi, J. Normand, K. Raghavachari, A. Rendell, J. C. Burant, S. S. Iyengar, J. Tomasi, M. Cossi, N. Rega, J. M. Millam, M. Klene, J. E. Knox, J. B. Cross, V. Bakken, C. Adamo, J. Jaramillo, R. Gomperts, R. E. Stratmann, O. Yazyev, A. J. Austin, R. Cammi, C. Pomelli, J. W. Ochterski, R. L. Martin, K. Morokuma, V. G. Zakrzewski, G. A. Voth, P. Salvador, J. J. Dannenberg, S. Dapprich, A. D. Daniels, Ö. Farkas, J. B. Foresman, J. V. Ortiz, J. Cioslowski, and D. J. Fox, Wallingford CT, 2009.

6. J. L. Bao and D. G. Truhlar, *Chem. Soc. Rev.*, 2017, **46**, 7548–7596.

7. Y. Zhao, I. Yavuz, M. Wang, M. H. Weber, M. Xu, J.-H. Lee, S. Tan, T. Huang, D. Meng, R. Wang, J. Xue, S.-J. Lee, S.-H. Bae, A. Zhang, S.-G. Choi, Y. Yin, J. Liu, T.-H. Han, Y. Shi, H. Ma, W. Yang, Q. Xing, Y. Zhou, P. Shi, S. Wang, E. Zhang, J. Bian, X. Pan, N.-G. Park, J.-W. Lee and Y. Yang, *Nat. Mater.*, 2022, **21**, 1396–1402.

8. D. Sheppard, P. Xiao, W. Chemelewski, D. D. Johnson and G. Henkelman, *J. Chem. Phys.*, 2012, **136**, 074103.

9. T. D. Kühne, M. Iannuzzi, M. Del Ben, V. V. Rybkin, P. Seewald, F. Stein, T. Laino, R. Z. Khaliullin, O. Schütt, F. Schiffmann, D. Golze, J. Wilhelm, S. Chulkov, M. H. Bani-Hashemian, V. Weber, U. Borštnik, M. Taillefumier, A. S. Jakobovits, A. Lazzaro, H. Pabst, T. Müller, R. Schade, M. Guidon, S. Andermatt, N. Holmberg, G. K. Schenter, A. Hehn, A. Bussy, F. Belleflamme, G. Tabacchi, A. Glöß, M. Lass, I. Bethune, C. J. Mundy, C. Plessl, M. Watkins, J. VandeVondele, M. Krack and J. Hutter, *J. Chem. Phys.*, 2020, **152**, 194103.

10. J. P. Perdew, K. Burke and M. Ernzerhof, *Phys. Rev. Lett.*, 1996, **77**, 3865–3868.

11. J. VandeVondele and J. Hutter, *J. Chem. Phys.*, 2007, **127**, 114105.

12. G. Bussi, D. Donadio and M. Parrinello, *J. Chem. Phys.*, 2007, **126**, 014101.

13. W. Humphrey, A. Dalke and K. Schulten, *J. Mol. Graph.*, 1996, **14**, 33–38.

14. S. Zhang, S. M. Hosseini, R. Gunder, A. Petsiuk, P. Caprioglio, C. M. Wolff, S. Shoaee, P. Meredith, S. Schorr, T. Unold, P. L. Burn, D. Neher and M. Stolterfoht, *Adv. Mater.*, 2019, **31**, 1901090.

15. Z. Liu, R. Lin, M. Wei, M. Yin, P. Wu, M. Li, L. Li, Y. Wang, G. Chen, V. Carnevali, L. Agosta, V. Slama, N. Lempesis, Z. Wang, M. Wang, Y. Deng, H. Luo, H. Gao, U. Rothlisberger, S. M. Zakeeruddin, X. Luo, Y. Liu, M. Grätzel and H. Tan, *Nat. Mater.*, 2025, **24**, 252–259.

16. W. Hui, L. Chao, H. Lu, F. Xia, Q. Wei, Z. Su, T. Niu, L. Tao, B. Du, D. Li, Y. Wang, H. Dong, S. Zuo, B. Li, W. Shi, X. Ran, P. Li, H. Zhang, Z. Wu, C. Ran, L. Song, G. Xing, X. Gao, J. Zhang, Y. Xia, Y. Chen and W. Huang, *Science*, 2021, **371**, 1359–1364.
17. M. V. Khenkin, E. A. Katz, A. Abate, G. Bardizza, J. J. Berry, C. Brabec, F. Brunetti, V. Bulovic, Q. Burlingame, A. Di Carlo, R. Cheacharoen, Y.-B. Cheng, A. Colsmann, S. Cros, K. Domanski, M. Dusza, C. J. Fell, S. R. Forrest, Y. Galagan, D. Di Girolamo, M. Graetzel, A. Hagfeldt, E. von Hauff, H. Hoppe, J. Kettle, H. Koebler, M. S. Leite, S. Liu, Y.-L. Loo, J. M. Luther, C.-Q. Ma, M. Madsen, M. Manceau, M. Matheron, M. McGehee, R. Meitzner, M. K. Nazeeruddin, A. F. Nogueira, C. Odabasi, A. Osherov, N.-G. Park, M. O. Reese, F. De Rossi, M. Saliba, U. S. Schubert, H. J. Snaith, S. D. Stranks, W. Tress, P. A. Troshin, V. Turkovic, S. Veenstra, I. Visoly-Fisher, A. Walsh, T. Watson, H. Xie, R. Yildirim, S. M. Zakeeruddin, K. Zhu and M. Lira-Cantu, *Nat. Energy*, 2020, **5**, 35–49.